Chemical routes to materials

Fe₂O₃/BiVO₄ heterogeneous photo-Fenton catalyst with excellent dye degradation performance prepared by ultrasonic-assisted calcination

Jingjing Li[1], Junhua You[1,*] , Zhiwei Wang[1], Yao Zhao[1], Jingsheng Xu[1], Mingyi Duan[2,*], and Hangzhou Zhang[2,*]

[1] *School of Materials Science and Engineering, Shenyang University of Technology, Shenyang 110870, China*
[2] *Department of Orthopedics, Joint Surgery and Sports Medicine, First Affiliated Hospital of China Medical University, Shenyang 110001, China*

ABSTRACT

A series of $Fe_2O_3/BiVO_4$ composite photo-Fenton catalysts were prepared by a simple ultrasonic-assisted calcination method. By changing the calcination temperature, FB-2 with tetragonal structure $BiVO_4$ has excellent photo-Fenton performance. The crystal structure and chemical composition of the composite catalyst were studied by a series of characterizations. Under 5 W LED illumination, 97% rhodamine B dye (Rh B) was degraded within 40 min in FB-2 sample, which was attributed to the high efficiency of photogenic electron–hole pair separation. The subsequent capture experiment and Tafel test proved that h^+, e^-, $\cdot OH$ were the main active substances in the degradation process and the flow direction of electrons in the reaction process. The composite catalyst has good cyclic stability and efficient photo-Fenton catalytic degradation performance, and has good reference value for the degradation of water dyes.

Introduction

With the rapid progress of industrialization in society, many water pollution problems have come along [1, 2], among which, dye pollution accounts for most of them. Generally speaking, dyes have complex structures, high molecular weights, are readily soluble in water, resist degradation, have potential carcinogenicity and mutagenicity. Therefore, dye-containing wastewater will directly destroy the ecological balance of water bodies and harm on human health [1].In order to solve the problem of dye pollution in water, the photo-Fenton process has been widely concerned. Under the condition of additional introduction of light, Fe^{2+} can not only accelerate the reduction of Fe^{3+}, but also directly photolysis H_2O_2 to produce $\cdot OH$. Therefore, the synergistic action of Fe^{2+} and light can produce more $\cdot OH$, thus improving the degradation efficiency of photo-Fenton.

BiVO$_4$ has three crystal forms: tetragonal zircon structure (t-z BiVO$_4$), tetragonal scheelite (t-s BiVO$_4$) and monoclinic scheelite (m-s BiVO$_4$) (Fig. 1a–c). The most studied BiVO$_4$ photocatalyst is the scheelite BiVO$_4$, with a band gap of 2.4 eV [2]. The crystal structure of m-s BiVO$_4$ is similar to that of t-s BiVO$_4$, and it has a scheelite structure. The Bi–O polyhedron in m-s BiVO$_4$ is more severely deformed by the 6S^2 lone pair of Bi^{3+} than the Bi–O polyhedron in t-s BiVO$_4$ [3], so m-s BiVO$_4$ exhibits higher photocatalytic performance [4].

In the field of photo-Fenton, Fe$_2$O$_3$ and BiVO$_4$ are both hot research materials in recent years. In these years, a series of two-dimensional photo-Fenton catalytic materials such as Fe$_2$O$_3$/BiVO$_4$ [5], Fe$_2$O$_3$/Bi$_2$WO$_6$ [6], and Fe$_2$O$_3$/Bi$_2$MoO$_6$ [7] have been prepared by simple method, which is effective for methylene blue (MB) and tetracycline (TC) have good degradation properties. The Fe$_2$O$_3$/BiOI [8] synthesized by the two-step hydrothermal emulsion polymerization method and the immersion precipitation method showed good degradation performance for methyl orange (MO), phenol and tetracycline hydrochloride (TCH). Therefore, it is a practical measure to use Fe$_2$O$_3$ as a Fenton catalyst to couple with a semiconductor photocatalyst matching the band gap to prepare a composite catalyst with good photo-Fenton performance.

Therefore, in this paper, Fe$_2$O$_3$/BiVO$_4$ two-dimensional composite photo-Fenton catalyst was prepared by ultrasound-assisted calcination for the first time in the field of photo-Fenton. A series of photo-Fenton catalysts with different crystal structures of BiVO$_4$ were prepared by adjusting the calcination temperature. Using rhodamine B (Rh B), MB and MO as target pollutants, the performance of Fe$_2$O$_3$/BiVO$_4$ composite photo-Fenton catalyst was tested, and the catalytic mechanism of the catalyst was further analyzed. The composite catalyst has high efficiency photo-Fenton catalytic performance

and has good reference value for the degradation of dyes in water.

Materials and methods

Bismuth nitrate pentahydrate (Bi(NO$_3$)$_3$·5H$_2$O), ammonium metavanadate (NH$_4$VO$_3$), ferric chloride hexahydrate (FeCl$_3$·6H$_2$O), sodium lauryl sulfate (C$_{12}$H$_{25}$SO$_4$Na) were purchased from Sinopharm Chemical Reagent Co. Ltd. (Shanghai, China). Rhodamine B (Rh B) was purchased from Shanghai Aladdin Industrial Company. All reagents are of analytical grade, and no further purification is required when used. All experiments use deionized water.

Synthesis of BiVO$_4$

The tetragonal BiVO$_4$ was synthesized following the reported literature [9]. 4 mmol (1.94 g) Bi(NO$_3$)$_3$·5H$_2$O and 4 mmol (0.468 g) NH$_4$VO$_3$ were dissolved in 50 mL of deionized water and stirred vigorously for 1 h at room temperature. The aqueous solution was then sonicated for an additional 1 h in a high-intensity ultrasonic bath. In an instant, the color of the precipitate turned yellow. The yellow precipitate was then washed with deionized water, centrifuged, and excess water molecules were removed with absolute ethanol, and then placed in an oven at 60 °C for 12 h. The powder material was calcined at 300 °C for 4 h, and the resulting bright yellow material was denoted as BiVO$_4$.

Synthesis of Fe$_2$O$_3$/BiVO$_4$ photo-Fenton catalysts

The Fe$_2$O$_3$/BiVO$_4$ was synthesized following the reported literature [10] (Fig. 2). 1 mmol (0.324 g) BiVO$_4$ was uniformly dispersed in 50 mL deionized water, then 3 mmol (0.81 g) FeCl$_3$·6H$_2$O and

Figure 1 **a**–**c** Crystal structure of BiVO$_4$ with tetragonal zircon structure, tetragonal scheelite structure and monoclinic scheelite structure.
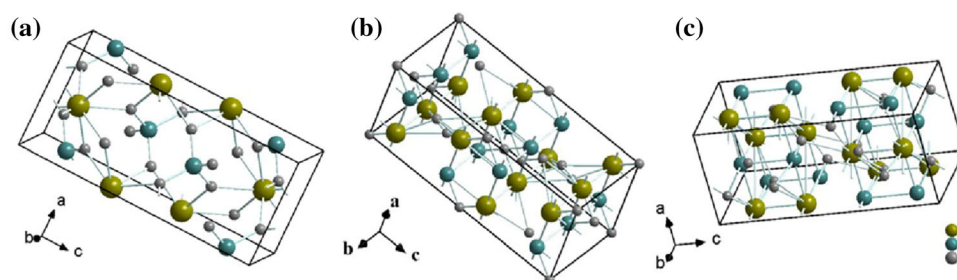
1.5 mmol (0.45 g) SDS were added, and ultrasonically treated for 2 h. Then remove excess water with ethanol. Put it in a 60 °C oven for 12 h, and heat the dried powder at 100 °C, 300 °C, 500 °C, and 700 °C for 4 h to remove the organic content. Substances obtained after calcination were designated as FB-1, FB-2, FB-3, and FB-4, respectively. For comparison, Fe_2O_3 could also be synthesized following a similar procedure.

Characterization

XRD patterns were obtained on a D/Max-RB X-ray diffractometer (Rigaku) with Cu Kα as scan rate (2θ) and irradiation at 5°/min in the range of 10°–80°. Powder morphologies were characterized using SEM (Zeiss Supra 55), HR-TEM (FEI Tecnai F30) and STEM techniques equipped with energy dispersive X-ray (EDX) compositional analysis. XPS measurements were performed on a PHI-5000 C ESCA system operating at 14.0 kV and 25 mA using a Mg Kα source. Fourier transform infrared spectra were measured between 400 and 4000 cm^{-1} using a Nicolet Aexus 470 infrared spectrometer with KBr as a reference background. Diffuse reflectance spectroscopy (DRS) was measured by UV–visible spectrophotometry (PERSEE T9), with $BaSO_4$ as the reference sample. The RF-5301PC fluorescence spectrometer was used for testing, and the specific parameters were: 150 W xenon lamp, wavelength measurement range of 340–750 nm, and wavelength moving speed of 20000 nm/min. Transient photocurrent, electrochemical impedance spectroscopy (EIS) and Mott–Schottky test (M–S), all in a three-electrode system (one ITO glass electrode (working electrode), platinum electrode (counter electrode) and saturated calomel electrode (SCE, reference electrode)) on a PARSTAT 2273 electrochemical workstation.

Photo-Fenton experiments

The degradation experiments of different dyes proved the catalytic activity of $Fe_2O_3/BiVO_4$ composite photo-Fenton catalysts. The photo-Fenton reaction was carried out in a PCX50A discover multi-channel photocatalytic reaction instrument produced by Beijing Perfect-light Technology Company. The photocatalytic reactor uses 9 LED lamps with a power of 5 W as the cold light source. During the reaction, the disc is set to rotate one grid per minute, thereby ensuring that each reaction vial is evenly irradiated with light. Usually, 0.1 g of the prepared photo-Fenton catalyst was added to 100 mL of dye solution (Rh B = 20 mg/L, MB = 35 mg/L, MO = 40 mg/L), and after 30 min adsorption under dark conditions, the dye was the adsorption–desorption equilibrium was reached with the catalyst sample. Then add a 5 W LED light source, and at the same time add an appropriate amount of H_2O_2 (30%). 4 mL of the suspension was taken at intervals and centrifuged to remove solid particles. The concentration of the dye was determined by UV–vis spectrophotometry (PERSEE T9) at the corresponding maximum absorbance. Where C_0 is the initial concentration of the dye, C is the dye concentration sampled at different times during the reaction process, the degradation efficiency of the composite photo-Fenton catalyst to organic pollutants was calculated by C/C_0, and the first-order kinetic curve ln (the relationship between C_0/C) and time t yields the photoreaction rate constant.

For the Fenton-like reaction process, except that the 5 W LED light source was not introduced, the rest of

Figure 2 Flow chart of preparation of BiVO$_4$/Fe$_2$O$_3$ composite photo-Fenton catalyst.
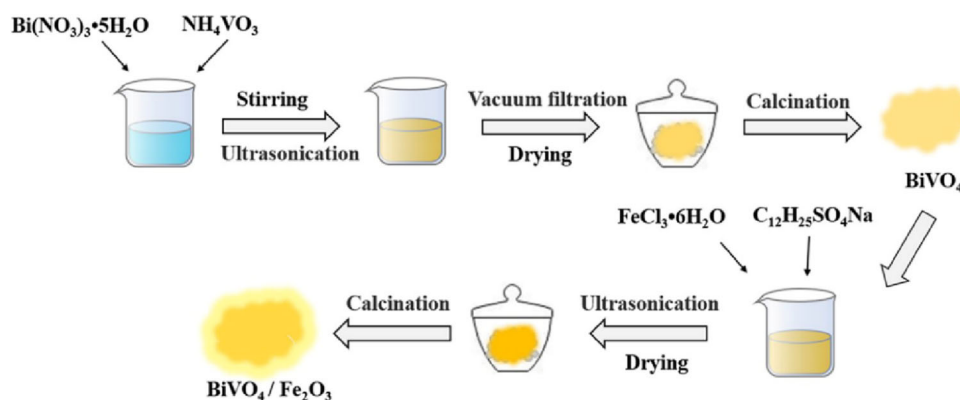
the experimental process was the same as the above operation. For the photocatalytic experiments, the rest of the experimental procedures were the same as those described above, except that no H_2O_2 was added.

Results

Morphologies and structures

First, the crystal structures of the as-prepared $BiVO_4$ and a series of $Fe_2O_3/BiVO_4$ (FB-1 ∼ FB-4) were characterized (Fig. 3a). The XRD pattern of pure $BiVO_4$ prepared by calcination at 300 °C was matched with that of tetragonal $BiVO_4$ (PDF# 14-0133) [9]. In 18.41°, 24.4°, 30.76°, 32.68°, 34.83°, 39.64°, 43.92°, 47.19°, 48.51° and 49.99° in the diffraction peak of respectively with (101), (200), (211), (112), (220), (301), (103), (321), (312), (400) crystal plane matching. Tetragonal $BiVO_4$ (PDF# 14-0133) corresponds to FB-1 and FB-2 prepared by calcination at 100 °C and 300 °C. Because monoclinic $BiVO_4$ and tetragonal $BiVO_4$ are calcined at 528 K, a reversible crystal phase transition [4] can occur, that is, from tetragonal $BiVO_4$ at low temperature to monoclinic $BiVO_4$. FB-3 and FB-4 were obtained by increasing the calcination

temperature at 500 °C and 700 °C. The diffraction peaks of the two at 18.8°, 28.92°, 30.64° and 53.34° are consistent with the monoclinic $BiVO_4$ (PDF# 14-0688) (011), (121), (040) and (161) planes, which is consistent with the previously reported view that calcination can change the crystal phase of $BiVO_4$ [6]. In the XRD patterns of FB-1 ∼ FB-4, no pronounced Fe_2O_3 diffraction peaks were observed, which may be related to its low content or poor crystallinity. However, the existence of Fe_2O_3 can be further confirmed by the surface element scanning of TEM. The characterization results of XRD can prove that by changing the calcination temperature, $BiVO_4$ with two different crystal phases are obtained, and Fe_2O_3 is compounded with $BiVO_4$ without changing the crystal structure of the original $BiVO_4$. Furthermore, no other diffraction peaks were observed, confirming the phase purity of all composites [11].

In order to study the chemical composition and chemical structure of the heterogeneous catalysts, the XPS technique was used for further analysis. Only the peaks of four elements, Bi, V, O, and Fe, were detected in the full spectrum in Fig. 3b, which proves that the prepared catalyst is of high purity. The characteristic peaks at 516.5 eV and 524.2 eV in Fig. 3c correspond to the V $2p_{3/2}$ and V $2p_{1/2}$ spin orbits of V^{5+}, respectively [12]. In the high-resolution
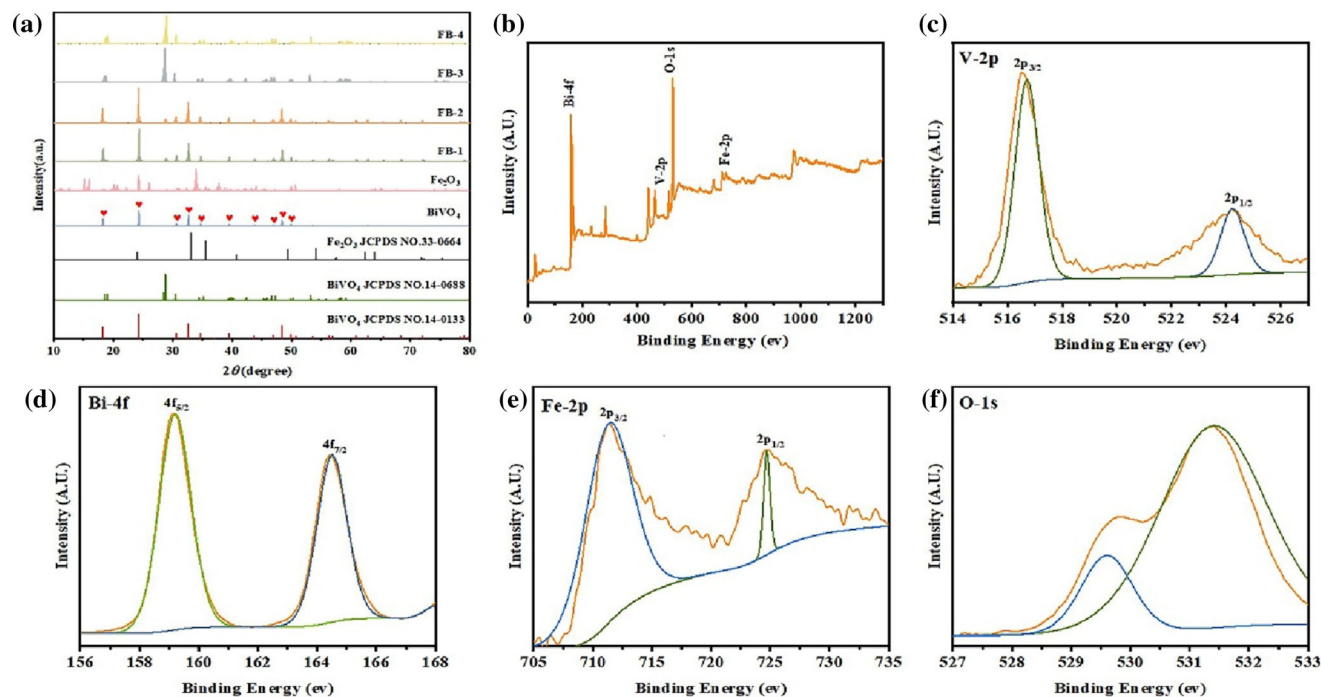

Figure 3 **a** XRD patterns of the prepared samples **b** XPS spectra of the total survey. **c**–**f** XPS diagram of V-2p, Bi-4f, Fe-2p and O-1 s.

XPS image of Bi 4f in Fig. 3d, Bi $4f_{5/2}$ and Bi $4f_{7/2}$ were observed to have two symmetrical characteristic peaks at 159.1 eV and 164.5 eV [13], which indicates that the primary element valence of Bi is Bi^{3+} [14]. The two distinct peaks at 711.3 eV and 724.7 eV in Fig. 3e belong to the Fe $2p_{3/2}$ and Fe $2p_{1/2}$ spin–orbit states [15] of Fe_2O_3 nanoparticles, respectively. In addition, the XPS spectrum of O 1s of $Fe_2O_3/BiVO_4$ is divided into two peaks around 529.8 eV and 531.3 eV (Fig. 3f), and an apparent binding energy peak is formed at 529.8 eV, which belongs to Bi–O in $BiVO_4$ and is centred at 531.3 eV. The rise belongs to the Fe_2O_3 species Fe–O [16]. The above results confirmed that $Fe_2O_3/BiVO_4$ nanocomposites were successfully prepared.

On this basis, the chemical composition and chemical structure of the composite catalyst was further confirmed by FT-IR (Fig. 4a). In the FT-IR of Fe_2O_3, 598 cm^{-1} corresponds to the stretching vibration of Fe–O [17], 1134 cm^{-1} corresponds to the characteristic absorption peak of Fe_2O_3 [18], and 1595 cm^{-1} corresponds to the N–H vibration [18] caused by the residual SDS in the preparation process, while 3404 cm^{-1} corresponds to the stretching vibration [19] of the hydroxyl group adsorbed on the surface of Fe_2O_3. The FT-IR of $BiVO_4$ at 736 cm^{-1} corresponds to the stretching vibration of VO_4^{3-} [20]. From the enlarged FT-IR image (Fig. 4b), it can be observed that the characteristic peak of VO_4^{3-} in the FB-1 ~ FB-4 composite catalyst has shifted and the intensity has decreased, which may be caused by the successful contact between Fe_2O_3 and $BiVO_4$ [18]. The
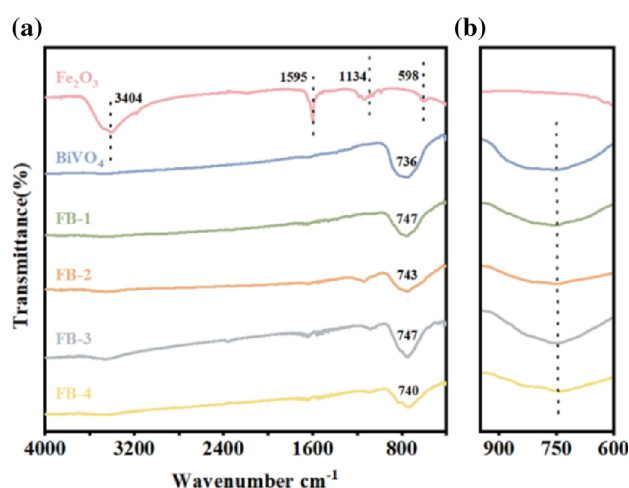
outflow of electrons from the conduction band of $BiVO_4$ will lead to changes in the local electronic structure [21], which corresponds to the mechanism explanation in the following part. Possibly due to the low loading content of Fe_2O_3, there is no prominent FT-IR diffraction peak of Fe_2O_3 in the FB-1 ~ FB-4 composites. The FT-IR characterization results are consistent with the XRD and XPS analysis results.

The morphologies and microstructures of Fe_2O_3, $BiVO_4$ and $Fe_2O_3/BiVO_4$ nanocomposites were observed by scanning electron microscopy (SEM) and transmission electron microscopy (TEM). Figure 5a, b are the SEM images of the Fe_2O_3 sample and the $BiVO_4$ sample, respectively. It can be seen that Fe_2O_3 is a varying block in a stacked state, while the $BiVO_4$ sample is a sphere with varying size and rough surface. Figure 5c–f shows the FB sample prepared under different temperature calcination, with an average size of about 1–2 μm. With the increase of the calcination temperature, the morphology of the FB sample gradually changed from regular spherical to irregular because more irregular Fe_2O_3 [10] would crystallize on the surface of the $BiVO_4$ sample during this process, covering the active sites on the surface of the $BiVO_4$ sample. Compared with the other three FB samples, FB-2 is smaller in size and closer in shape to regular spherical particles, which is similar to the $BiVO_4$ sample [9]. The SEM–EDS (Supplementary Fig. S1) analysis results show that Bi, V, Fe, and O are well distributed in their respective regions [22], which agrees with the XRD analysis results. As depicted by the TEM image in Fig. 5g, h, the interplanar distances are 0.16 and 0.27 nm, matching Fe_2O_3 (121) and $BiVO_4$ (400), respectively.

Photoelectric properties

The absorbance of the initial samples and composite samples were characterized by UV–vis diffuse reflectance spectroscopy (UV–vis DRS), and the results are shown in Fig. 6a. The absorption sideband of $BiVO_4$ is 530 nm, which is in line with a previous report [9]. Fe_2O_3 exhibits broad absorption up to 700 nm due to transitions in the d orbital [23], indicating high activity in the visible region. Furthermore, due to the lower Fe_2O_3 content in the FB samples, the FB composites exhibited similar absorption properties to pure $BiVO_4$. The recombined FB-2 ~ FB-4 all undergo a red shift, attributed to the charge transition between Fe_2O_3 and $BiVO_4$ [24]. This
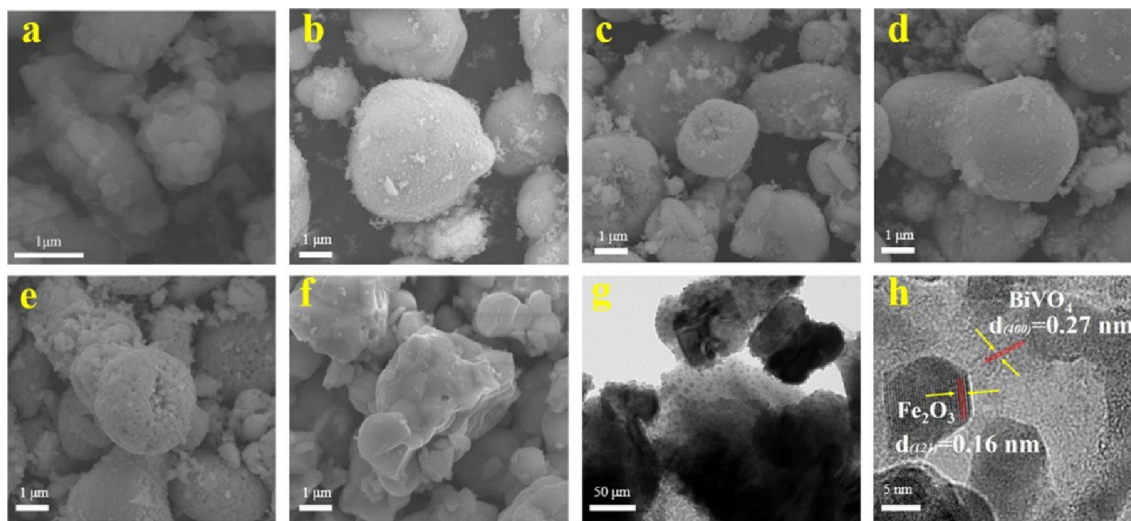

Figure 4 **a**, **b** FT-IR image and partial enlarged image of the prepared sample.

Figure 5 **a**–**f** SEM images of Fe_2O_3, $BiVO_4$ and FB series samples, **g**, **h** TEM of FB-2.

indicates that the photo-response range has been expanded, and more photoinduced electrons and holes can be excited to form [14], that is, the utilization of visible light by the composite sample is enhanced. Calculate the band gap value of the semiconductor according to the Kubelka–Munk formula (Eq. 1) [25], where A is the absorption coefficient, h is Planck's constant, and v is optical frequency, E_g is the band gap, and the value of n depends on the semiconductor type.
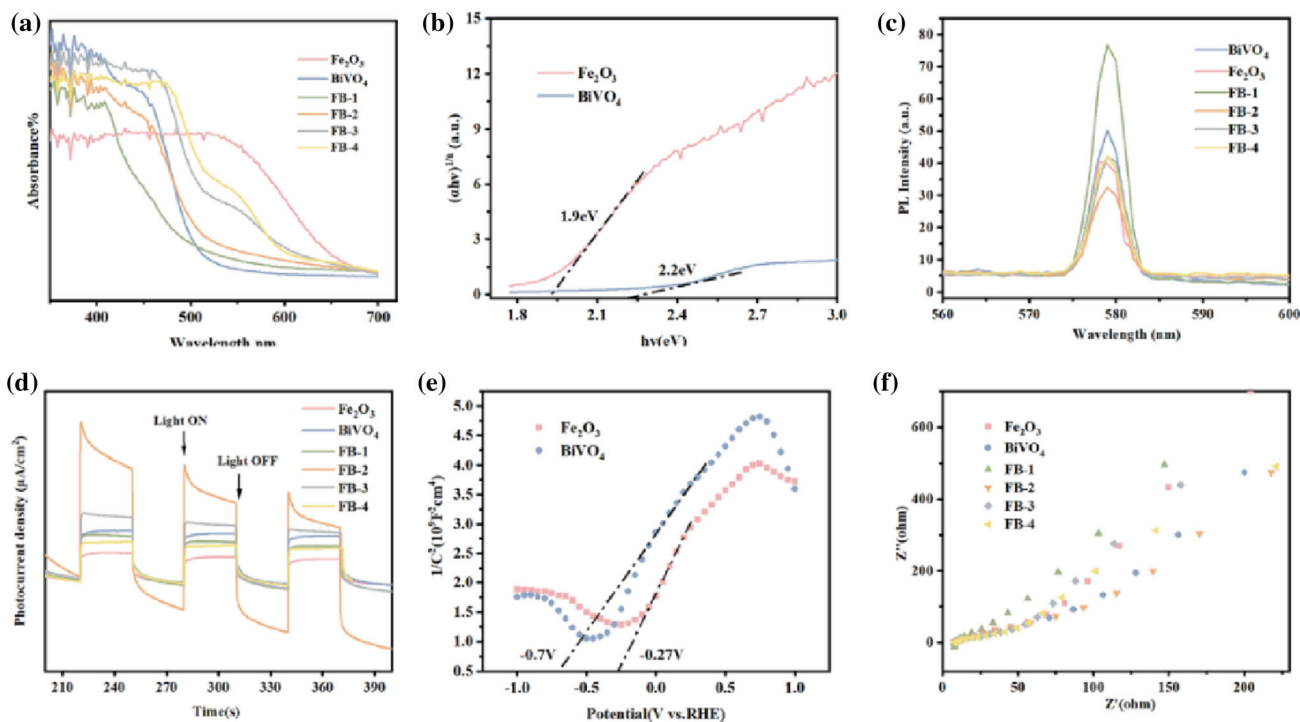

Figure 6 **a** UV–Vis diffuse reflectance spectra of Fe_2O_3, $BiVO_4$ and FB series samples. **b** Estimate the band gap values of Fe_2O_3 and $BiVO_4$ based on the plotted $(\alpha h v)^{1/2}$ versus $h v$. **c** PL emission spectra (the excitation wavelength is 340 nm). **d** Transient photocurrent curves of prepared samples. **e**, **f** Mott-Schottky and EIS curves of the prepared samples (in a three-electrode system with ITO glass electrode as working electrode, platinum electrode as counter electrode and saturated calomel electrode as reference electrode. 0.5 M Na_2SO_4 solution was used as electrolyte solution).

$$\alpha h v = A \left(h v - E_g \right)^{n/2}, \tag{1}$$

BiVO$_4$ and Fe$_2$O$_3$ are direct-gap semiconductors and indirect-gap semiconductors, respectively, with n values of 2 and 1/2 [14]. The material's band gap [21] was estimated from the inflexion point between the tangent line on the inflexion point and the horizontal line, and the band gaps (E$_g$) of BiVO$_4$ and Fe$_2$O$_3$ were determined to be 2.2 eV and 1.9 eV, respectively (Fig. 6b). The band gap of composite samples FB-1 ∼ FB-4 is between 2.04 and 2.14 eV (Fig. S2a, b), which is smaller than that of pure BiVO$_4$ samples.

Photoluminescence spectroscopy can study the efficiency of photogenerated carrier recombination and separation. The results of photoluminescence spectroscopy can reveal electron–hole pair transfer, migration and recombination processes [26]. When the semiconductor is illuminated by light, the catalyst generates electrons and holes, and the fluorescence emission spectrum represents the released energy of some of the electrons and holes recombination. Higher emissivity indicates better charge recombination efficiency. The emission spectra of Fe$_2$O$_3$ and BiVO$_4$ show higher intensities (Fig. 6c), indicating that the electron–hole pairs of Fe$_2$O$_3$ and BiVO$_4$ are rapidly recombined. As expected, the PL intensity of the FB-2 composite is lower than that of Fe$_2$O$_3$ and BiVO$_4$. Therefore, the FB-2 composite structure is illustrated to facilitate the efficient separation of electron–hole pairs, which is consistent with the optical properties of DRS [27].

Figure 6d compares the transient photocurrent densities of the obtained BiVO$_4$, Fe$_2$O$_3$ and a series of FB electrodes under visible light irradiation. All electrodes produced a fast photocurrent response when the light was present. Then, when the light is cut off, it instantly drops to zero, these materials are photosensitive. Under visible light irradiation, the photocurrent of FB-2 was significantly higher than pure BiVO$_4$. These results show that BiVO$_4$ has a higher photogenerated electron and hole combination rate than FB-2. That is, FB-2 has efficient charge separation, consistent with the results of PL spectroscopy [28].

It is well known that the photocatalytic activity of a catalyst is closely related to its band structure and charge transfer kinetics. The band structures of the samples were prepared, and their charge transfer and recombination properties were analyzed. First, the flat-band potential of the sample was measured using M–S. Figure 6e is the M–S curve of the measured sample. The slopes of Fe$_2$O$_3$ and BiVO$_4$ are positive, indicating that the semiconductor is n-type, consistent with the results reported in the previous literature [18]. Meanwhile, the flat-band potentials (approximately equal to the conduction band in n-type semiconductors) of Fe$_2$O$_3$ and BiVO$_4$ materials are − 0.27 V and − 0.7 V, respectively (relative to a common hydrogen electrode (RHE)). In general, the bottom of the conduction band of an n-type semiconductor is 0.1 V [29] minus the flat band potential. Therefore, the conduction band potentials of Fe$_2$O$_3$ and BiVO$_4$ materials are − 0.37 V and − 0.8 V, respectively (relative to standard hydrogen electrode (RHE)). After that, the conduction band values of Fe$_2$O$_3$ and BiVO$_4$ materials close to normal hydrogen electrode (NHE) were calculated according to Eq. (2) [30], which were − 0.78 V and − 1.21 V, respectively.

$$E_{RHE} = E_{NHE} + 0.059 \, pH \tag{2}$$

$$E_{VB} = E_g + E_{CB} \tag{3}$$

Combined with the above DRS test, the band gap values of Fe$_2$O$_3$ and BiVO$_4$ materials are 1.9 eV and 2.2 eV, respectively. Therefore, according to Eq. (3), the valence band positions of Fe$_2$O$_3$ and BiVO$_4$ materials are further calculated to be 1.12 eV and 0.99 eV, respectively. In summary, the specific energy band structure values of Fe$_2$O$_3$ and BiVO$_4$ materials are shown in Table 1.

The changes in charge separation and transfer in the FB composite were further determined by electrochemical impedance spectroscopy (EIS). The smaller the diameter of the semicircle in the EIS diagram, the faster the electron mobility and the more efficient the separation of carriers [17]. The semicircle diameter of the FB-2 composite sample in Fig. 6f is much smaller than that of the other composite samples, indicating that the FB-2 interfacial layer resistance is reduced, which is beneficial to charge separation and transfer.

The above series of photoelectric performance characterizations further confirmed the successful preparation of Fe$_2$O$_3$/BiVO$_4$ composite photo-Fenton materials. The prepared FB-2 sample has excellent photo-response performance and efficient electron transfer efficiency. This is inseparable from its excellent photo-Fenton degradation efficiency below.

Table 1 Specific band structure values of Fe_2O_3 and $BiVO_4$ prepared

	Fe_2O_3	$BiVO_4$
$E_{fB(RHE)}$	− 0.27 V	− 0.7 V
$E_{CB(RHE)}$	− 0.37 V	− 0.8 V
$E_{CB(NHE)}$	− 0.78 V	− 1.21 V
E_g	1.9 eV	2.2 eV
E_{VB}	1.12 V	0.99 V

Photo-Fenton catalytic performance

Taking the degradation of Rh B as an example, the performance of other photo-Fenton catalysts was evaluated. Under the condition of adding an appropriate amount of Fe_2O_3, different calcination temperatures have different affect the photo-Fenton performance of the prepared catalysts. With Rh B as the target pollutant, FB-2 calcined at 300 °C had the highest photo-Fenton degradation efficiency (Fig. 7a). As the calcination temperature increased, more Fe_2O_3 nanoparticles were crystallized, covering the active sites on the FB surface. Moreover, the accumulation of excess Fe_2O_3 nanoparticles due to unbalanced forces hinders the efficient formation of heterojunctions [31], which results in the ineffective separation of photogenerated carriers and reduces the catalytic activity. In addition, the photo-Fenton degradation kinetics curves of FB-1 $\sim$ FB-4 can be approximated as a quasi-first-order process: $\ln(C_0/C) = kt$. By fitting the obtained $\ln(C_0/C)$ curve, the photoreaction rate constant k was obtained (Fig. 7c), in which the photodegradation rate of FB-2 was the highest, reaching 0.086 min^{-1}.

In Fig. 7d, the concentration changes of Rh B under different degradation time during the photo-Fenton degradation of Rh B by FB-2 were monitored. With the increase of illumination times, the characteristic peak intensity of Rh B decreased continuously. After 60 min, the absorption peak almost disappeared. The final degradation rate of the FB-1 $\sim$ FB-4 samples can be observed in the bar graph of Fig. 7b, and the broken line in the figure intuitively reflects the changing trend of the degradation rate. It is further confirmed that FB-2 has excellent photo-Fenton degradation performance. Supplementary Fig. S3a–c show the photo-Fenton, Fenton-like and photocatalytic degradation performance curves of $BiVO_4$,

Fe_2O_3 and composite FB-2 for Rh B. The photo-Fenton performance of the composite FB-2 was significantly improved (Fig. 7e), and the degradation rate of Rh B reached 97% within 40 min. It is proved that the FB-2 composite sample obtained by calcination of $BiVO_4$ loaded with an appropriate amount of Fe_2O_3 at 300 °C can promote the separation and migration of photogenerated carriers. At the same time, the exposure of more active sites enables the photocatalytic and Fenton oxidation has the best synergistic effect. It is also proved that the photocatalytic response of $BiVO_4$ is dominant in the Fenton-photocatalytic synergistic reaction of FB-2.

It is generally believed that the cyclic stability of catalysts is one of the critical signs of good catalytic performance. The catalytic stability of FB-2 catalyst for five consecutive degradations of Rh B (20 mg L^{-1}) under visible light was investigated. After five photo-Fenton catalytic cycles, the FB-2 composite catalyst still has good degradation performance (Fig. 7f), confirming the good long-term reusability of the FB-2 catalyst, which proposed a new idea for the practical industrial application of composite catalyst.

It is generally believed that the photo-Fenton catalysis reaction is carried out on the surface of the catalyst, so the positive and negative charges on the surface of the catalyst will directly affect the adsorption process of the catalyst to the dye molecules, thereby affecting the catalytic effect of the photo-Fenton [32]. In this experiment, FB-2 has good degradation performance on Rh B and MB cationic dyes. However, the anionic dye MO did not achieve the expected effect. It is speculated that the surface of the FB-2 catalyst has many negative charges. At the moment of adding the cationic dyes (Rh B and MB), the negative charges on the catalyst's surface quickly attract the cationic dyes. When the light source is introduced, and H_2O_2 is added, the cationic dyes adsorbed on the catalyst surface rapidly undergo a series of redox reactions with H_2O_2. They are degraded (Fig. 8a, d).

To clarify the photo-Fenton reaction mechanism of the catalyst, the effects of H_2O_2 dosage (Fig. 8b) and catalyst dosage (Fig. 8c) on the degradation performance of Rh B were discussed. Figure 8b shows the degradation efficiency of Rh B (20 mg L^{-1}) by FB-2 by adding different amounts of H_2O_2. It can be seen that the decomposition rate of Rh B increases significantly with the increase in the quantity of H_2O_2 added. From the fitted first-order kinetic line graph (Fig. 8e)
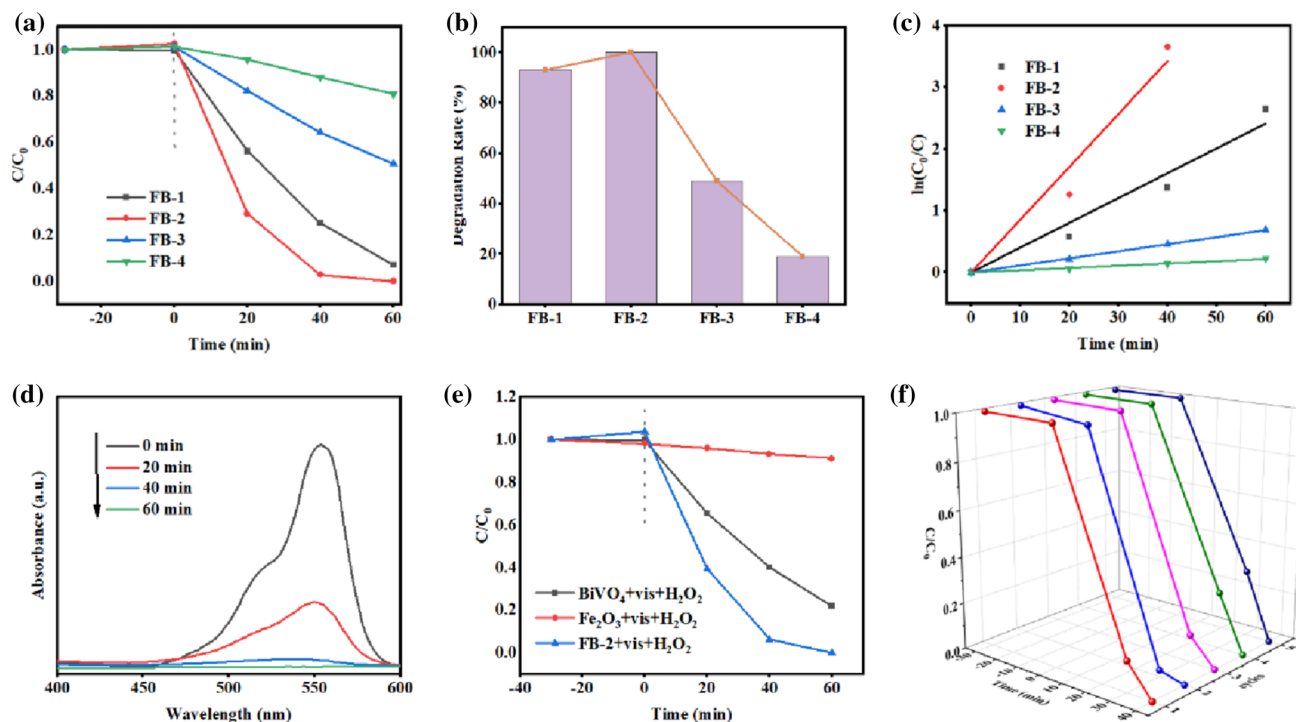
Figure 7 a, **b** FB-1 ∼ FB-4 photo-Fenton degradation performance curve and degradation rate histogram **c** First-order kinetic curves of FB-1 ∼ FB-4 after fitting **d** UV absorbance at different times during photo-Fenton degradation of FB-2 sample **e** photo-Fenton properties of $BiVO_4$, Fe_2O_3 and FB-2 **f** photo-Fenton cycle test of the FB-2 sample.

and the corresponding kinetic constant bar graph (Supplementary Fig. S4a), it can be seen that as the H_2O_2 dosage increases from 0 to 1 mL, the fitted rate constant rapidly increased to 0.07731 min^{-1}. This is because with the addition of H_2O_2, the generation rate of ·OH is accelerated, promoting the degradation of the target pollutants. However, when more than 1 mL of H_2O_2 was added, the fitted rate constant decreased from 0.07731 to 0.06162 min^{-1}. This may be because excess H_2O_2 captures ·OH [Eq. (4)], resulting in a continuous increase in the degradation rate of ·OH, and many HO_2· is also generated. Compared with ·OH, the oxidation potential of HO_2· is lower, which inhibits the entire photo-Fenton reaction process [Eq. (5)], in turn, reduces the rate of pollutant degradation [33].

$$H_2O_2 + ·OH \rightarrow HO_2^· + H_2O \qquad (4)$$

$$HO_2^· + ·OH \rightarrow H_2O + O_2 \qquad (5)$$
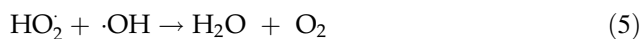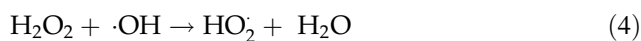
Usually, the catalyst degradation rate increases with the increase of catalyst dosage. According to the fitted first-order kinetic line (Fig. 8f) and the corresponding kinetic constant histogram (Supplementary Fig. S4b), as the catalyst dosage increased from 0.04 to

0.08 g, its fitted rate constant Increased from 0.07336 to 0.11745 min^{-1}. However, when the dosage continued to increase, the fitted rate consistent decreased to 0.06021 min^{-1}, which may be due to the decrease of the transmittance of the solution due to the excess catalyst, which reduced the photocatalytic efficiency of $BiVO_4$ and hindered the electron from $BiVO_4$ flows to Fe_2O_3, which in turn reduces the photo-Fenton catalytic degradation efficiency of the composite catalyst.

Mechanism of catalyst performance improvement

To study the experimental mechanism of the Fe_2O_3/ $BiVO_4$ photo-Fenton reaction, a capture experiment was carried out to determine the active species that played a significant role in the response process. In the photo-Fenton reaction, silver nitrate ($AgNO_3$), isopropanol (IPA), ethylenediaminetetraacetic acid disodium salt (EDTA-2Na) and p-benzoquinone (BQ) were used as trapping agents for e^-, ·OH, h^+ and $O_2^{·-}$, respectively [34] (Fig. 9a). Among them, IPA, EDTA-2Na, and BQ inhibited the degradation rate of the catalyst to the dye by 60%, 60%, and 24%,
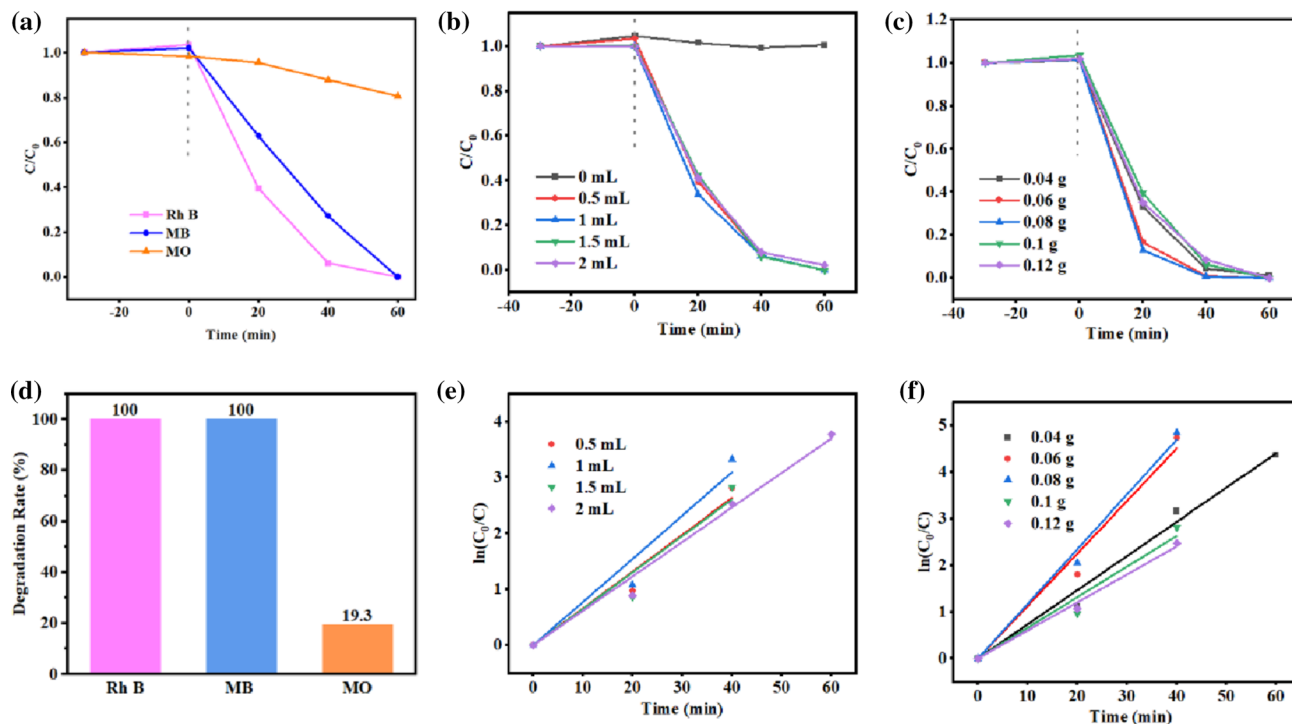
Figure 8 **a**, **d** Photo-Fenton degradation performance curves and bar graphs of FB-2 for different dyes (Rh B, MB, MO) **b**, **c** the effects of different H_2O_2 dosage and catalyst content on the photo-Fenton performance of FB-2 samples **e**, **f** corresponding fitting first-order kinetic linear diagram of photo-Fenton degradation performance of FB-2 samples with different H_2O_2 dosage and catalyst content.

respectively (Fig. 9b). The results of capture experiments showed that e^- and ·OH were involved in the photo-Fenton reaction, and h^+ was the main active species in the photo-Fenton reaction, which played a crucial role in the degradation of Rh B. When BQ was added to the photo-Fenton reaction, there was a slight inhibitory effect during the reaction. It is speculated that the addition of BQ may reduce solution's transparency, thereby inhibiting the degradation efficiency of the catalyst. However, the degradation efficiency of Rh B did not change in the end, indicating that $O_2\cdot^-$ was not the active species in the reaction process.

To judge the electron flow direction between Fe_2O_3 and $BiVO_4$, the Tafel curves of Fe_2O_3 and $BiVO_4$ under light and without light were tested (Fig. 9c). Under visible light irradiation, the redox equilibrium potential of $BiVO_4$ shifted to a more negative direction [13] and the redox potential of Fe_2O_3 moves in a more positive direction. Under visible light irradiation, $BiVO_4$ has a more negative redox equilibrium potential than Fe_2O_3, indicating that $BiVO_4$ has a higher surface electron energy level in Na_2SO_4 solution under visible light irradiation [13]. At the same time, it can be seen that the redox properties of Fe_2O_3 are more affected by visible light irradiation, indicating that the energy level structure of Fe_2O_3 is more affected by minority carrier injection. The open-circuit voltages of $Fe_2O_3/BiVO_4$ under dark and light conditions were measured to be -0.88 V and -0.81 V, respectively. These open circuit voltages lie between the redox potentials of Fe_2O_3 and $BiVO_4$, representing the flow of electrons from $BiVO_4$ to Fe_2O_3 during photo-Fenton catalysis.

Based on the above series of photoelectric characterization, performance testing experiments, trapping experiments and Tafel curves, the electron flow diagram during the reaction of the FB-2 composite photo-Fenton catalyst (Fig. 9d, f) and the reaction mechanism of Rh B degradation (Fig. 10) are proposed. Under illumination, $BiVO_4$ and Fe_2O_3 are excited to generate photogenerated electrons (e^-) and holes (h^+) simultaneously [Eq. (6)]. Since the conduction band and valence band of $BiVO_4$ are more negative than Fe_2O_3, the e^- on the conduction band can be easily transferred to the conduction band of Fe_2O_3 which is closer to it (Fig. 9e), further reducing Fe^{3+} to Fe^{2+} [Eq. (7)], the Fe^{2+} generated by the
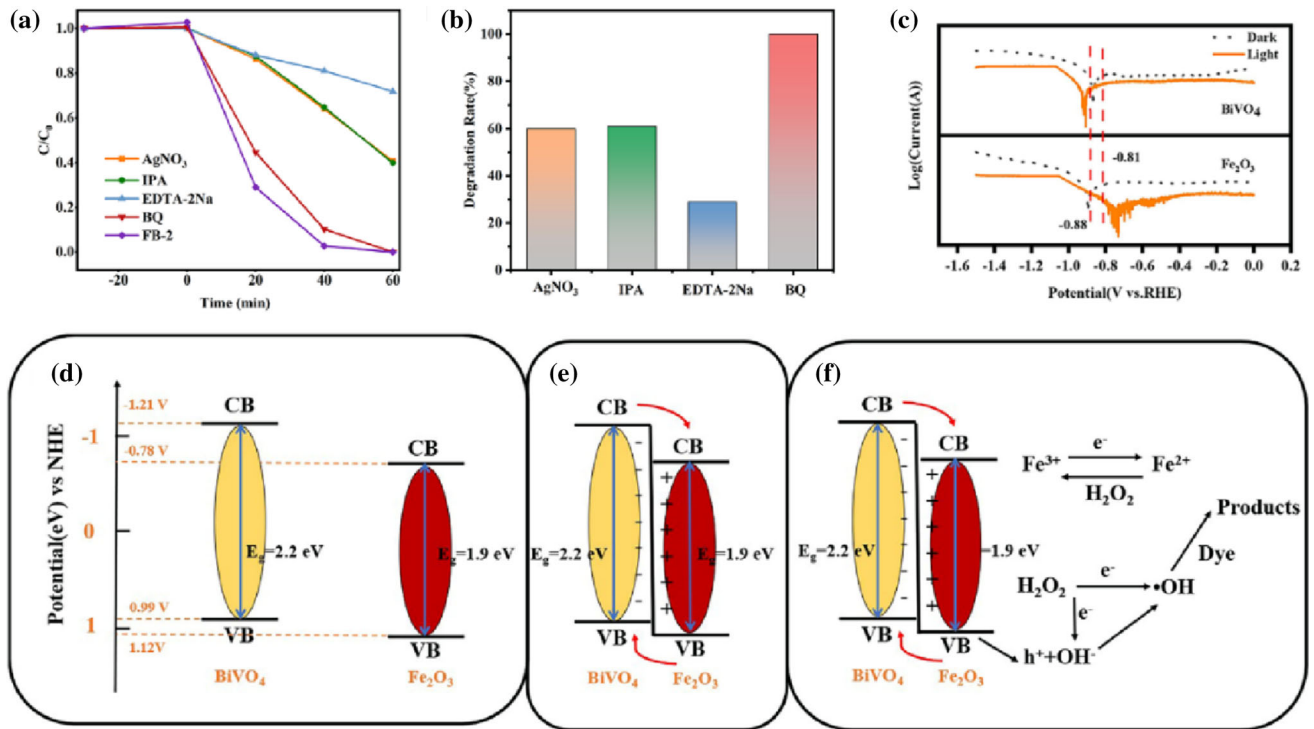
Figure 9 **a**, **b** The capture experiment of FB-2 by different scavengers and the corresponding degradation rate histogram **c** Tafel curves of $BiVO_4$ and Fe_2O_3 under light and no light conditions. **d**, **f** Electron flow diagram during $Fe_2O_3/BiVO_4$ photo-Fenton catalyst reaction.

reduction reaction reacts with H_2O_2 to generate ·OH active species that participate in the photo-Fenton reaction to degrade Rh B [Eq. (9), (11)]. The added H_2O_2 can not only oxidize the generated Fe^{2+} to Fe^{3+} (Eq. (9)), but also react with e^- to generate ·OH active species to promote the degradation of the dye [Eq. (8)]. At the same time, the holes in the valence band of Fe_2O_3 can also react with the OH^- generated

by the decomposition of H_2O_2 to generate ·OH to promote the degradation of pollutants [Eq. (10)] (Fig. 9f). The $Fe_2O_3/BiVO_4$ photo-Fenton catalyst system accelerates the transfer of electrons and promotes the cycle between Fe^{3+} and Fe^{2+}, thereby improving the catalytic degradation efficiency of the FB-2 composite photo-Fenton catalyst.

Figure 10 Reaction mechanism diagram of $Fe_2O_3/BiVO_4$ composite photo-Fenton catalyst.
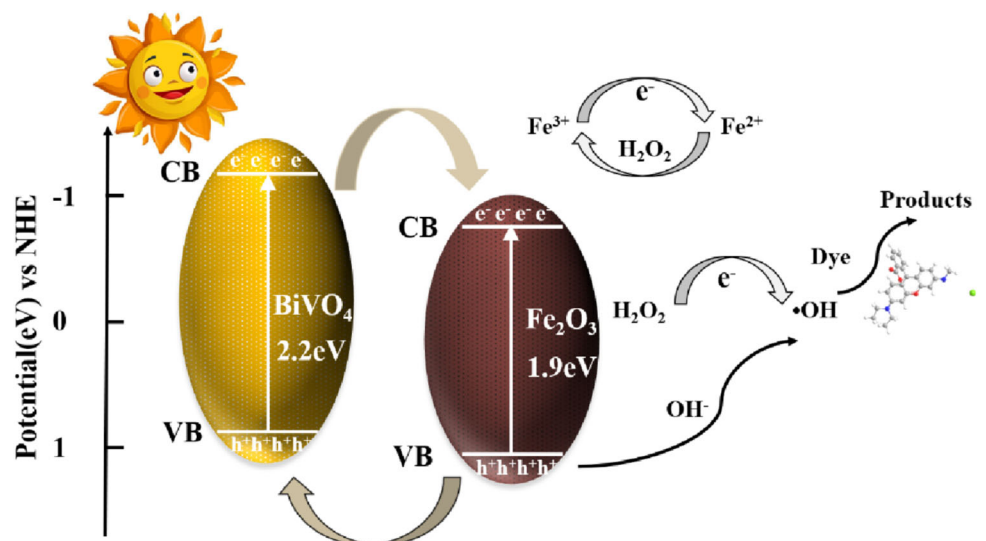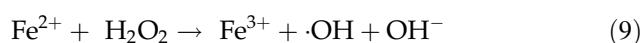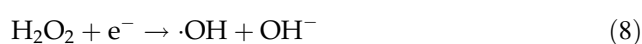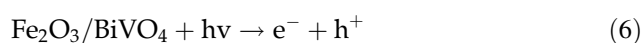
Table 2 Summary of properties of BiVO₄–Fe₂O₃ composites

Catalyst	Target pollutants	Light source	Degradation time/efficiency	Application field	References
Fe$_2$O$_3$/BiVO$_4$	MB (10 mg/L)	300 W Xenon lamp	40 min/100%	Photo-Fenton	[5]
	Rh B (15 mg/L)		30 min/98.4%		
Fe$_2$O$_3$/BiVO$_4$	TC (20 mg/L)	300 W Xenon lamp	120 min/75.8%	Photocatalytic	[14]
Fe$_2$O$_3$/BiVO$_4$	4-NP (0.4 mmol/L)	300 W Xenon lamp	30 min/98%	Photocatalytic	[35]
Fe$_2$O$_3$/BiVO$_4$	Rh B (20 mg/L)	5 W LED lamp	40 min/97%	Photo-Fenton	This work
	MB (35 mg/L)		40 min/80%		

$$Fe_2O_3/BiVO_4 + h\nu \rightarrow e^- + h^+ \tag{6}$$

$$Fe^{3+} + e^- \rightarrow Fe^{2+} \tag{7}$$

$$H_2O_2 + e^- \rightarrow \cdot OH + OH^- \tag{8}$$

$$Fe^{2+} + H_2O_2 \rightarrow Fe^{3+} + \cdot OH + OH^- \tag{9}$$

$$h^+ + OH^- \rightarrow \cdot OH \tag{10}$$

$$Dye + \cdot OH \rightarrow CO_2 + H_2O \tag{11}$$

Discussion

In this paper, the photo-Fenton catalyst with high catalytic degradation performance was prepared by ultrasound-assisted calcination. FB-2 with tetragonal BiVO₄ structure was obtained by calcination at 300 °C with the best photo-Fenton degradation performance. The capture experiment and Tafel test proved that h⁺, e⁻ and ·OH were the main active species in the reaction process and the specific direction of electrons in the reaction process.

Compared with other Fe₂O₃/BiVO₄ photocatalytic degradation experiments (Table 2), under the irradiation of a weak light source (5 W LED) in this experiment, Rh B (20 mg/L) and MB (35 mg/L) dyes still have good degradation efficiency within 40 min. That is, under low-intensity light, the FB-2 composite photo-Fenton catalyst prepared in this experiment still has good catalytic degradation activity.

Conclusions

Fe₂O₃/BiVO₄ composite photo-Fenton catalyst was prepared by a simple ultrasonic-assisted calcination method. The change of calcination temperature affects the photo-Fenton performance of FB series composite catalysts. FB-2 with tetragonal BiVO₄ structure, which was calcined at 300 °C, degraded 97% of Rh B (20 mg L⁻¹) within 40 min, and maintained high activity after five cycles of testing. The capture experiment and Tafel test further demonstrated the main active species and electron flow between catalyst interfaces during the reaction. The close interfacial contact and efficient charge transfer between Fe₂O₃ and BiVO₄ greatly enhance the synergistic reaction between them. At the same time, it provides a new idea and solution for the practical application of Fe₂O₃ based heterogeneous photo-Fenton catalyst.

Author contributions

JL: Conceptualization, methodology, data curation, writing—original draft. JY: Funding acquisition. ZW: Validation. YZ: Formal analysis. JX: Resources. MD: Supervision. HZ: Project administration.

Data and code availability

The date that support the findings of this study are available from the corresponding author upon reasonable request.

Declarations

Conflicts of interest All authors disclosed no relevant relationships.

Ethical approval Not Applicable.

Supplementary Information: The online version contains supplementary material available at https://doi.org/10.1007/s10853-023-08683-1.

References

[1] Hitam CNC, Jalil AA (2020) A review on exploration of Fe_2O_3 photocatalyst towards degradation of dyes and organic contaminants. J Environ Manag 258:110050. https://doi.org/10.1016/j.jenvman.2019.110050

[2] Xu M, Yang J, Sun C, Liu L, Cui Y, Liang B (2020) Performance enhancement strategies of bi-based photocatalysts: a review on recent progress. Chem Eng J. https://doi.org/10.1016/j.cej.2020.124402

[3] Li J, You J, Wang Z et al (2022) Application of α-Fe_2O_3-based heterogeneous photo-Fenton catalyst in wastewater treatment: a review of recent advances. J Environ Chem Eng. https://doi.org/10.1016/j.jece.2022.108329

[4] Tokunaga S, Kato H, Kudo A (2001) Selective preparation of monoclinic and tetragonal $BiVO_4$ with scheelite structure and their photocatalytic properties. Chem Mater 13:4624–4628. https://doi.org/10.1021/cm0103390

[5] Wen Y, Zhao Y, Guo M, Xu Y (2019) Synergetic effect of Fe_2O_3 and $BiVO_4$ as photocatalyst nanocomposites for improved photo-Fenton catalytic activity. J Mater Sci 54:8236–8246. https://doi.org/10.1007/s10853-019-03511-x

[6] Wang W, Zhao W, Zhang H, Dou X, Shi H (2021) 2D/2D step-scheme α-Fe_2O_3/Bi_2WO_6 photocatalyst with efficient charge transfer for enhanced photo-Fenton catalytic activity. Chin J Catal 42:97–106. https://doi.org/10.1016/s1872-2067(20)63602-6

[7] Wang W, Zhao W, Huang H, Chen R, Shi H (2021) A 2D/2D S-scheme photo-Fenton catalyst based on ultrathin Bi_2MoO_6 and Fe_2O_3 hexagonal nanosheets for efficient tetracycline degradation. Catal Sci Technol 11:2948–2956. https://doi.org/10.1039/d1cy00051a

[8] Jiang J, Gao J, Li T et al (2019) Visible-light-driven photo-Fenton reaction with α-Fe_2O_3/BiOI at near neutral pH: boosted photogenerated charge separation, optimum operating parameters and mechanism insight. J Colloid Interface Sci 554:531–543. https://doi.org/10.1016/j.jcis.2019.07.038

[9] Zhou L, Wang W, Liu S, Zhang L, Xu H, Zhu W (2006) A sonochemical route to visible-light-driven high-activity $BiVO_4$ photocatalyst. J Mol Catal A Chem 252:120–124. https://doi.org/10.1016/j.molcata.2006.01.052

[10] Hao C, Feng F, Wang X et al (2015) The preparation of Fe_2O_3 nanoparticles by liquid phase-based ultrasonic-assisted method and its application as enzyme-free sensor for the detection of H_2O_2. RSC Adv 5:21161–21169. https://doi.org/10.1039/c4ra17226d

[11] Liu S, Tang H, Zhou H, Dai G, Wang W (2017) Photocatalytic performance of sandwich-like $BiVO_4$ sheets by microwave assisted synthesis. Appl Surf Sci 391:542–547. https://doi.org/10.1016/j.apsusc.2016.06.184

[12] Ji K, Dai H, Deng J et al (2015) 3DOM $BiVO_4$ supported silver bromide and noble metals: high-performance photocatalysts for the visible-light-driven degradation of 4-chlorophenol. Appl Catal B 168–169:274–282. https://doi.org/10.1016/j.apcatb.2014.12.045

[13] Guo R, Yan A, Xu J et al (2020) Effects of morphology on the visible-light-driven photocatalytic and bactericidal properties of $BiVO_4$/CdS heterojunctions: a discussion on photocatalysis mechanism. J Alloys Compd. https://doi.org/10.1016/j.jallcom.2019.153246

[14] Ma C, Lee J, Kim Y, Cheol Seo W, Jung H, Yang W (2021) Rational design of α-Fe_2O_3 nanocubes supported $BiVO_4$ Z-scheme photocatalyst for photocatalytic degradation of antibiotic under visible light. J Colloid Interface Sci 581:514–522. https://doi.org/10.1016/j.jcis.2020.07.127

[15] Yamashita T, Hayes P (2008) Analysis of XPS spectra of Fe^{2+} and Fe^{3+} ions in oxide materials. Appl Surf Sci 254:2441–2449. https://doi.org/10.1016/j.apsusc.2007.09.063

[16] Gao X, Ma C, Liu Y, Xing L, Yan Y (2019) Self-induced Fenton reaction constructed by Fe (III) grafted $BiVO_4$ nanosheets with improved photocatalytic performance and mechanism insight. Appl Surf Sci 467–468:673–683. https://doi.org/10.1016/j.apsusc.2018.10.172

[17] Xie T, Zhang Y, Yao W, Liu Y, Wang H, Wu Z (2019) Synthesis of Bi-deficient monolayered Bi_2WO_6 nanosheets with enhanced photocatalytic activity under visible light irradiation. Catal Sci Technol 9:1178–1188. https://doi.org/10.1039/c8cy02344a

[18] Liu N, Ouyang D, Cai Y, Li Y (2020) Heterostructured Fe_2O_3/$BiVO_4$ nano-photocatalyst for the reduction of nitroarenes into amines. Ceram Int 46:24534–24543. https://doi.org/10.1016/j.ceramint.2020.06.240

[19] Liu Y, Ge HY, Zhang XZ, Huang SF, Cheng X (2013) Surface chemical modification and characterization of nano Fe_2O_3. Appl Mech Mater 345:180–183. https://doi.org/10.4028/www.scientific.net/AMM.345.180

[20] Gotić M, Musić S, Ivanda M, Šoufek M, Popović S (2005) Synthesis and characterisation of bismuth (III) vanadate.

J Mol Struct 744–747:535–570. https://doi.org/10.1016/j.molstruc.2004.10.075

[21] Xi J, Xia H, Ning X et al (2019) Carbon-intercalated 0D/2D hybrid of hematite quantum dots/graphitic carbon nitride nanosheets as superior catalyst for advanced oxidation. Small 15:e1902744. https://doi.org/10.1002/smll.201902744

[22] Xu T, Zhu R, Zhu G et al (2017) Mechanisms for the enhanced photo-Fenton activity of ferrihydrite modified with BiVO$_4$ at neutral pH. Appl Catal B 212:50–58. https://doi.org/10.1016/j.apcatb.2017.04.064

[23] Zhou L, Wang L, Zhang J, Lei J, Liu Y (2016) Well-dispersed Fe$_2$O$_3$ nanoparticles on g-C$_3$N$_4$for efficient and stable photo-fenton photocatalysis under visible-light irradiation. Eur J Inorg Chem 2016:5387–5392. https://doi.org/10.1002/ejic.201600959

[24] Sahar S, Zeb A, Liu Y, Ullah N, Xu A (2017) Enhanced Fenton, photo-Fenton and peroxidase-like activity and stability over Fe$_3$O$_4$/g-C$_3$N$_4$ nanocomposites. Chin J Catal 38:2110–2119. https://doi.org/10.1016/s1872-2067(17)62957-7

[25] Zhao Y, Tao C, Xiao G et al (2016) Controlled synthesis and photocatalysis of sea urchin-like Fe$_3$O$_4$@TiO$_2$@Ag nanocomposites. Nanoscale 8:5313–5326. https://doi.org/10.1039/c5nr08624h

[26] Wei B, Wang C, He Y, Ran G, Song Q (2021) A novel FeS$_2$@g-C$_3$N$_4$ composite with enhanced photo-Fenton catalytic activity for pollutant degradation. Compos Commun. https://doi.org/10.1016/j.coco.2021.100652

[27] Wang T, Liu X, Men Q et al (2019) Photocatalytic removal using g-C$_3$N$_4$ quantum dots/Bi$_2$Ti$_2$O$_7$ composites. Spectrochim Acta A Mol Biomol Spectrosc 213:19–27. https://doi.org/10.1016/j.saa.2019.01.051

[28] Zhang M, Zhang Y, Tang L et al (2019) Ultrathin Bi$_2$WO$_6$ nanosheets loaded g-C$_3$N$_4$ quantum dots: a direct Z-scheme photocatalyst with enhanced photocatalytic activity towards degradation of organic pollutants under wide spectrum light irradiation. J Colloid Interface Sci 539:654–664. https://doi.org/10.1016/j.jcis.2018.12.112

[29] Liu L, Hu P, Cui W, Li X, Zhang Z (2017) Increased photocatalytic hydrogen evolution and stability over nano-sheet g-C$_3$N$_4$ hybridized CdS core@shell structure. Int J Hydrog Energy 42:17435–17445. https://doi.org/10.1016/j.ijhydene.2017.02.171

[30] Bornoz P, Prevot MS, Yu X, Guijarro N, Sivula K (2015) Direct light-driven water oxidation by a ladder-type conjugated polymer photoanode. J Am Chem Soc 137:15338–15341. https://doi.org/10.1021/jacs.5b05724

[31] Chakraborty A, Sarangapany S, Mishra U, Mohanty K (2021) Green synthesized magnetically separable iron oxide nanoparticles for efficient heterogeneous photo-Fenton degradation of dye pollutants. J Clust Sci 33:675. https://doi.org/10.1007/s10876-021-02010-x

[32] Xu H, Wu L, Jin L, Wu K (2017) Synthesis of Fe$_2$O$_3$/TiO$_2$ monoliths for the enhanced degradation of industrial dye and pesticide via photo-Fenton catalysis. J Mater Sci Technol 33:30–38. https://doi.org/10.1016/j.jmst.2016.04.008

[33] Singh J, Sharma S, Aanchal, Basu S (2019) Synthesis of Fe$_2$O$_3$/TiO$_2$ monoliths for the enhanced degradation of industrial dye and pesticide via photo-Fenton catalysis. J Photochem Photobiol A Chem 376:32–42. https://doi.org/10.1016/j.jphotochem.2019.03.004

[34] Liu X, Xu J, Ni Z, Wang R, You J, Guo R (2019) Adsorption and visible-light-driven photocatalytic properties of Ag$_3$PO$_4$/WO$_3$ composites: a discussion of the mechanism. Chem Eng J 356:22–33. https://doi.org/10.1016/j.cej.2018.09.001

[35] Zhang K, Liu Y, Deng J et al (2017) Fe$_2$O$_3$/3DOM BiVO$_4$: high-performance photocatalysts for the visible light-driven degradation of 4-nitrophenol. Appl Catal B 202:569–579. https://doi.org/10.1016/j.apcatb.2016.09.069